

Identification of Intervening Materials in Gamma-ray Spectroscopy Measurements Using Angularly Deconvolved Spectra With Multiple Sources in the Field-of-View

David Goodman, Michael Streicher, Yuefeng Zhu, Zhong He, *Senior Member, IEEE*

Abstract— The mass thickness and atomic number of materials shielding radioactive sources emitting multiple resolvable gamma-ray energies can be characterized by measuring the attenuation and Compton scatter of emitted gamma-rays in recorded spectra against estimated values for a suite of materials and thicknesses. Compton imaging using a Maximum Likelihood Expectation Maximization (MLEM) based reconstruction can be used to separate angular spectra allowing simultaneous characterization of multiple shielded sources. Using the described algorithm on experimental ^{133}Ba data we demonstrate estimation of mass thickness and atomic number for iron, tin and lead shields with another bare source in the field-of-view with average standard error of 0.6 g/cm^2 and 1.5 respectively while an aluminum shield is reconstructed with ambiguous atomic number but correct thickness.

Index Terms—3D CdZnTe detectors, angular spectrum determination, Compton imaging, MLEM reconstruction, shielding characterization

I. INTRODUCTION

Unknown shielding configurations hinder source characterization when an object emitting gamma-rays is found in the field. After a particular isotope has been detected and identified, effective object shielding can be estimated by measuring the spectral modulation of source gamma-rays as they traverse shielding [1]. Once object shielding has been characterized, improved, shielding corrected estimates of source parameters, such as activity, can be made. Recently gamma-ray imaging spectrometers, which allow estimation of directional gamma-ray spectra, have become common commercially and in research [2][3][4][5]. Spectrum based shielding identification algorithms can be applied on directional gamma-ray spectra extracted through imaging. This expands the capabilities of imaging spectrometers beyond that of traditional spectrometers, enabling source detection and shielding characterization as a function of angle. Imaging spectrometers therefore better handle realistic measurement scenarios, such as when multiple sources of the same isotope are simultaneously shielded by differing materials, where traditional spectrometers cannot provide any angularly resolved detail. This novel, angularly resolved shielding information can then be leveraged by users to better respond to unknown objects found in the field.

For shielded sources, emitted gamma-ray spectra are convolved with an unknown shielding response function that

changes the measured photopeak ratios through photoelectric absorption and Compton scatter. A previous common technique employed by GADRAS uses complicated detector response models to estimate source shielding from shielding modulated spectra [6]. However, as controlled software, GADRAS has limited availability to the community. The alternative, simple technique used in this paper estimates shielding thickness ρx and effective atomic number Z from spectra by measuring both shielding Compton scatter and the modulation of known, photopeak ratios [1]. However, all non-imaging shielding identification algorithms fail when multiple sources of the same isotope are in the field-of-view (FOV) simultaneously, each with its own distinct shielding, leading to an angularly integrated spectrum from all sources and incorrect estimated shielding. This unwanted angular integration complicates realistic source geometries, and can be solved by detangling directional spectra through gamma-ray imaging.

One simple form of gamma-ray imaging involves raster scanning a mechanical collimator across the FOV. The collimator limits the detector's angular response, avoiding unwanted angular integration and separating source spectra, at the expense of measurement efficiency. Instead Compton imaging, where the incident direction of gamma-rays can be localized to the surface of a cone, can be used to simultaneously measure the spectra of multiple sources without loss of efficiency.

Traditional simple back-projection, where Compton cones from all events are linearly summed, does not sufficiently separate neighboring source spectra due to angular blur from the detector response. Blur from detector response can be deconvolved using Maximum Likelihood Expectation Maximization (MLEM) based techniques, reducing spectral contamination from neighboring sources, to improve calculation of angular spectra. Angular gamma-ray spectra have been previously computed using energy-imaging integrated spectral deconvolution (EIID), a MLEM based technique, which solves for the source distribution, in both energy and angular space, most likely to produce the given measurement [7][8]. Deconvolved, EIID spectra have been used to coarsely estimate shielding thickness and atomic number using photopeak attenuation as a function of energy for individual sources [9]. However, this EIID implementation did not leverage the information contained in gamma-rays that Compton scatter in shielding. Furthermore, EIID is computationally expensive and requires large amounts of computer memory. The alternative imaging algorithm described in this work is computationally cheaper, only reconstructing angular source intensities in several spec-

D. Goodman, M. Streicher, Y. Zhu and Z. He are with the Department of Nuclear Engineering and Radiological Sciences, University of Michigan, Ann Arbor, MI 48109 USA (email: digoodma@umich.edu).

tral bins, assuming full energy deposition of each incident gamma-ray. This contrasts with EIID where all possible gamma-ray energies above the recorded energy for each event are considered, allowing for reconstruction of partial energy deposition events. However, this large associated increase in computational cost does not greatly improve directional spectra for moderate gamma-ray energies where most events are full energy deposition. Running the shielding identification algorithm described in [1] on directional gamma-ray spectra calculated using this simple MLEM imaging technique allows for accurate reconstruction of effective angular shielding configurations, $Z(\theta, \phi)$ and $\rho x(\theta, \phi)$, with multiple sources simultaneously in the FOV in near real time on personal computers. This work illustrates the novel application of a recent shielding identification algorithm on directional, gamma-ray spectra extracted via Compton imaging on a fieldable, digital CdZnTe system.

II. SHIELDING IDENTIFICATION ALGORITHM

High energy resolution spectrometers allow extraction of shielding information from recorded spectra. Combining the complimentary information contained in photopeak ratios and small-angle Compton scatter probabilities allows simultaneous measurement of shielding mass thickness and atomic number. A detailed discussion of the algorithm can be found in [1] for uranium and plutonium measurements while a brief summary is provided below.

A. Modulation of Emitted Peak Ratios

Gamma-rays are attenuated exponentially by shielding material. Given the emission of gamma-rays with energy E_1 and E_2 the attenuated fluxes through shielding of thickness x are calculated as

$$I_1 = I_1^0 e^{-(\frac{\mu}{\rho})_1 \cdot \rho x}, \quad I_2 = I_2^0 e^{-(\frac{\mu}{\rho})_2 \cdot \rho x} \quad (1)$$

where I_1^0 and I_2^0 are the initial fluxes, μ_1 and μ_2 are the shielding linear attenuation coefficients at each energy, x is the thickness of intervening material and ρ is the shielding density [10]. Given tabulated cross sections for each element Z , mass attenuation coefficients $(\frac{\mu}{\rho})_{2,Z}$ and $(\frac{\mu}{\rho})_{1,Z}$ can be calculated. Residuals between measured and predicted photopeak ratios can be calculated via

$$r_{\rho x, Z}^2 = \left[\ln\left(\frac{I_1}{I_2}\right) - \ln\left(\frac{I_1^0}{I_2^0}\right) - \left[\left(\frac{\mu}{\rho}\right)_{2,Z} - \left(\frac{\mu}{\rho}\right)_{1,Z} \right] \rho x \right]^2 \quad (2)$$

as a function of mass thickness ρx . N peak ratio residuals can then be combined into a single metric

$$R_{\rho x, Z}^2 = \sum_{k=1}^N \frac{r_{\rho x, Z, k}^2}{\sigma_k^2} \quad (3)$$

where $r_{\rho x, Z, k}$ is the k^{th} photopeak ratio residual with propagated variance σ_k^2 .

B. Small Angle Compton Scatter

Gamma-rays undergo small-angle Compton scatter in shielding with probability dictated by the Klein-Nishina formula [11]. The probability a gamma-ray small-angle Compton scatters in shielding of thickness D into a small-angle $d\Omega$ and then exits without subsequent interaction is

$$P_C = e^{-\mu_t D} \int_0^D \mu_t dx \int_{\Omega_D} \frac{1}{\sigma_t} \frac{d\sigma_c}{d\Omega} d\Omega \quad (4)$$

where μ_t is the shield linear attenuation coefficient, σ_t is the total interaction cross section, Ω_D is the subset of detectable scatter angles and $\frac{d\sigma_c}{d\Omega}$ is the Klein-Nishina cross section. Note this simplification assumes that the shielding attenuation of the incident and small-angled scattered gamma-ray are similar. Comparing this to the probability of a photon being unattenuated P_U we find

$$\frac{P_C}{P_U} = \mu_t D \frac{1}{\sigma_t} \int_{\Omega_D} \frac{d\sigma_c}{d\Omega} d\Omega \propto \rho D \frac{Z}{uA} \quad (5)$$

where A is the relative shielding atomic number and u is the atomic mass unit. Note the final simplification is possible as the Klein-Nishina cross section is proportional to the effective atomic number of the shield. This probability is measured via net counts

$$\frac{P_C}{P_U} = \frac{(A_C - B) - \beta(A_{PP} - B)}{A_{PP} - B} \quad (6)$$

where A_C is the gross small-angle Compton scatter counts, A_{PP} is gross photopeak counts, B is gross background counts and β is a system, self-small-angle scatter correction that is subtracted off. In practice, β stems from both scatter in the non-detector volume of the CdZnTe system and low energy tailing from true, non-scattered, photopeak events due to the pixelated readout used. Furthermore, self-scattered gamma-rays from the source container will contribute to β in thickly encapsulated sources.

Compton scatter residuals can be similarly calculated by computing the squared difference between the measured ratio of small-angle Compton scatter and unattenuated gamma-rays to the expected ratio as a function of shielding mass thickness and atomic number using tabulated data. Compton scatter residuals are then combined with photopeak ratio residuals to estimate Z and ρx of the intervening material. Regions of low, residual fit across all ratios imply plausible shielding configurations, as shown for a tin shielded ^{133}Ba source in Fig. 1. The intersection of the lowest residual fit from combined photopeak attenuation and Compton scattering is chosen as the estimated shielding thickness and atomic number.

III. IMAGING TECHNIQUE: COMPTON SPECTRAL ISOLATION

Gamma-rays below 1.02 MeV interact with detectors through Compton scattering and photoelectric absorption. The incident direction of Compton scattered gamma-rays that are

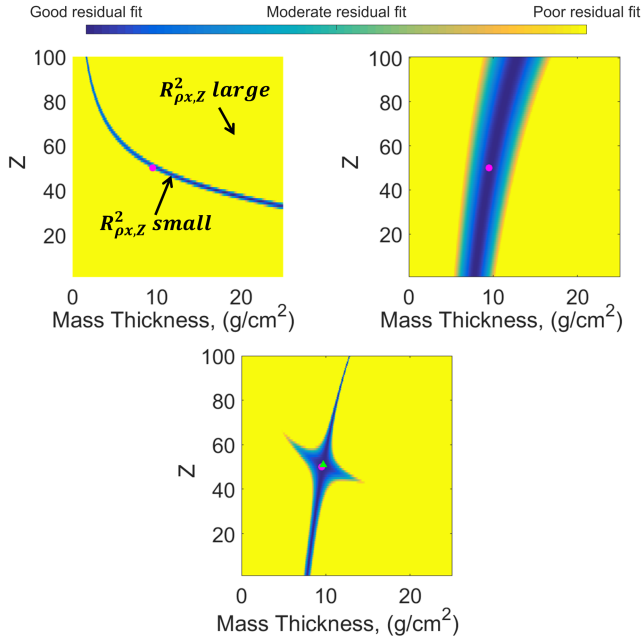


Fig. 1. Photopeak ratio (left), small-angle Compton scatter (right) and combined (bottom) residual fits calculated using the spectrum of a ^{133}Ba source shielded by 1.3 cm of tin. Note the complimentary information contained in photopeak ratio and Compton scatter residuals. Colormaps are independently scaled between images to maintain contrast. True shielding parameters are marked with a magenta dot while the intersection of photopeak and Compton scatter residuals, corresponding to estimated shielding parameters, is labeled with a green 'x'.

subsequently absorbed can be constrained through the Compton scatter formula

$$\cos(\theta) = 1 - \frac{E_1 m_e c^2}{E_0 E'} \quad (7)$$

where θ is the gamma-ray scatter angle, E_1 is the energy deposited in the first interaction, E' is the outgoing gamma-ray energy, $m_e c^2$ is the electron rest mass and E_0 is the initial gamma-ray energy [12]. Cones from many events are back-projected to a 2D sphere surrounding the detector, where they intersect as rings and are summed linearly: this corresponds to simple back-projection (SBP) where event responses are summed across the imaging domain without attempting to deconvolve the detector response [3]. Rings from gamma-rays sharing a common emission point overlap forming hotspots allowing directional spectra determination. Compton imaging system response dictated by finite energy and position resolution of CdZnTe systems causes point spread functions (PSF) with full-width-at-half-maximums of roughly 35° . This causes severe spectral leakage where counts from one source will contaminate another. This spectral contamination will bias the estimated angular spectra and therefore the photopeak and Compton scatter ratios.

A Maximum Likelihood Expectation Maximization (MLEM) based algorithm can be used to deconvolve blur induced from detector response in Compton imaging [13][14]. This greatly reduces the spectral contamination of neighboring sources by deconvolving PSFs to produce tight reconstructed, angular source distributions. Estimates of directional spectra

can then be extracted from these tightened reconstructions. In list-mode reconstruction, a pixel-by-pixel source intensity estimate, for a given energy bin $[E - dE, E + dE]$, is solved iteratively

$$\lambda_j^{n+1} = \frac{\lambda_j^n}{s_j} \sum_{i=1}^I \frac{t_{ij}}{\sum_{k=1}^J t_{ik} \lambda_k^n} \quad (8)$$

where λ_j^n is the intensity estimate of image pixel j during iteration n to gamma-rays of energy E , t_{ij} is the probability of recording event i given the photon was emitted from image pixel j , s_j is the system sensitivity to events emitted from image pixel j given J image pixels and I total events. Rows of the system matrix $t_{i\cdot}$ corresponding to Compton cones, blurred by the quadrature sum of angular uncertainties induced by limited position and energy resolution, are shown in Fig. 2 [15]. Sensitivity, omitting the effects of non-detector attenuation, was assumed uniform across the FOV within each energy bin and initial estimates λ^0 were seeded by summing the system matrix. Twenty five MLEM iterations were run on each energy bin of interest and directional intensities, assuming two source regions, C_1 and C_2 were extracted via summing reconstructed pixel intensities

$$C_1 = \sum_{j \in R_1} \lambda_j^{25}, \quad C_2 = \sum_{j \in R_2} \lambda_j^{25} \quad (9)$$

where R_1 and R_2 were the 20 most intense pixels within human-defined source regions. Note this corresponds to a small, 1.6% of the entire 4π imaging space on a 25 by 50 bin angular image grid. 20 pixels were chosen within the source region of interest as they contained a majority of the reconstructed source intensity while maintaining angular separation between hotspots. Total recorded counts I_{tot} within an energy bin, including non-imagable events, were allocated to either source I_1^{ML} or I_2^{ML} based on the fractional imaged hotspot intensities

$$I_1^{ML} = I_{tot} \frac{C_1}{C_1 + C_2}, \quad I_2^{ML} = I_{tot} \frac{C_2}{C_1 + C_2}. \quad (10)$$

The ratio between C_1 and C_2 was found to be relatively insensitive to the number of image pixels summed in each region of interest: at most, a 4% perturbation was seen changing the number of summed pixels between 15 and 25. Non-imageable events, such as events with only a single interaction, correspond to events for which a Compton cone cannot be reconstructed. However, the imagable event fraction is relatively constant over all possible incident directions. Net photopeak counts were calculated by subtracting off similarly allocated background at energies immediately higher than the photopeak. The photopeak, small-angle Compton scatter and background energy bins used in MLEM reconstructions for ^{133}Ba were listed in Fig. 5. A single, small-angle Compton scatter region was chosen from a prominent high energy peak to avoid the complication of subtracting off Compton continua from higher energy peaks. MLEM and SBP reconstructions of photopeak and small-angle Compton scatter energy bins during simultaneous measurement of bare and lead shielded ^{133}Ba sources are shown Fig. 3.

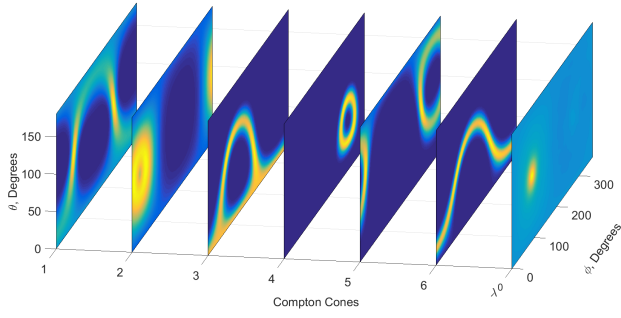


Fig. 2. Compton cones for six gamma-ray events corresponding to individual rows of the system matrix. All imageable events were summed together for the first MLEM estimate λ^0 . Images are scaled by individual maxima to maintain visual contrast.

MLEM reconstructed net counts were used to compute photopeak ratios and the small-angle Compton scatter probabilities used in the shielding identification algorithm as a function of direction. To correct for angular sensitivity as a function of energy using Compton imaging, MLEM reconstructed initial peak ratios were measured using bare sources. MLEM reconstructed small-angle Compton scatter probabilities were similarly measured as a function of angle using bare sources. Angular variation in small-angle scatter and photopeak ratios for bare sources stems from complicated attenuation and scatter in non-detector system components such as circuit boards and detector housing which is not included in the calculation of s_j . Comparing shielded measurements to bare cases cancels these non-source shielding contributions to the small-angle scatter and photopeak ratios. 12 and 20% relative fluctuations in MLEM reconstructed initial peak ratios and Compton scatter probabilities were seen across the FOV used in the measurement.

IV. DETECTOR SYSTEM

The Orion Prototype detector developed at the University of Michigan was used to measure all source configurations [16]. Orion consists of a 2×2 array of $2 \times 2 \times 1.5 \text{ cm}^3$ CdZnTe crystals inside an aluminum housing. Each crystal, with 11×11 pixelated anodes and a single planar cathode, is read out independently by a VAD_UM v1.2 digital ASIC [17]. Detector pixels are read out in coincidence allowing detection of multiple gamma-ray interactions within a single or across multiple crystals. This allows Compton imaging of gamma-rays that interact multiple times within the system. Sub-anode pixel interaction locations are computed by using ratios of transient signals induced on non-collecting, neighboring pixels. System energy and position resolution for ^{137}Cs gamma-rays are 0.63% and roughly $300 \mu\text{m}$ full-width-at-half-max (FWHM) respectively [16][18].

V. EXPERIMENTAL SETUP

A $90 \mu\text{Ci}$ ^{133}Ba source was placed 38 cm above the cathode side of the CdZnTe detectors at two locations corresponding to $(\theta, \phi) = (90^\circ, 90^\circ)$ and $(\theta, \phi) = (139^\circ, 108^\circ)$ in polar coordinates. Plates of various thickness and elemental composition were then placed between the source and detector in

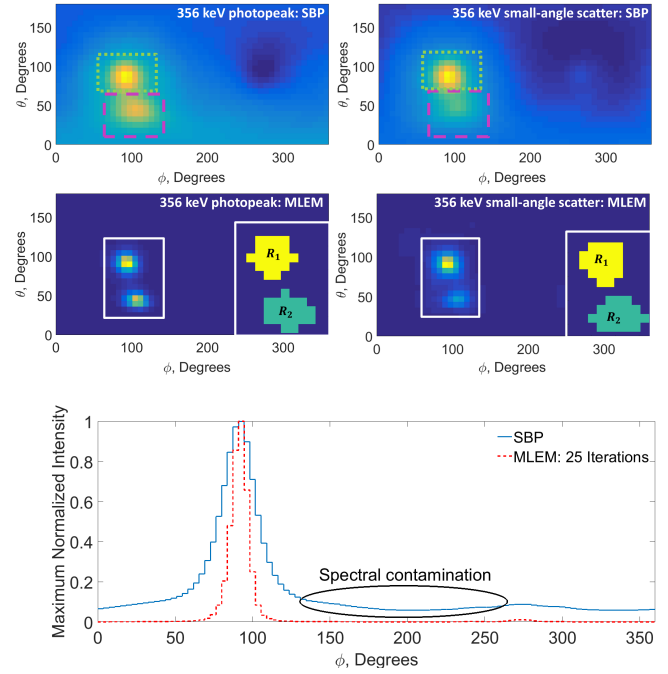


Fig. 3. (Top) Simple back-projection reconstructions of photopeak and small-angle scatter energy bins of interest for a combined lead shielded and bare ^{133}Ba measurement. The human defined lead and bare source regions are outlined with dashed and dotted lines respectively. Clear spectral contamination is seen in both directions as source PSFs overlap. (Middle) MLEM reconstructions of the same data. Note the improved angular separation between sources. Gross counts within source regions for each energy window are computed by summing the intensity of the 20 most intense pixels shown in the inset regions of interest. Images were scaled by individual maxima to maintain visual contrast. (Bottom) Azimuthal slices through SBP and MLEM reconstructions of the same bare source. Note the wider FWHM and non-zero baseline of the SBP reconstruction which contributes to spectral contamination.

addition to the bare cases as shown in Fig. 4. Plate shields were placed directly under the sources such that roughly all scatter angles less than 180° were possible while source to detector distance was kept roughly constant. Bare sources were measured for 8 hours while shielded sources were measured for 16 hours. Measurements were linearly combined to mimic the simultaneous measurement of multiple sources: individual count rates were low enough such that differences in dead-time and system performance from the simulated increased count rate from combining measurements were small. Individual measurement spectra illustrating modulation of peak ratios and small-angle Compton scatter are shown in Fig. 5.

VI. RESULTS

Combined bare and shielded ^{133}Ba measurements were reconstructed using MLEM on a discretized, 25 by 50, angular grid to estimate directional spectra and angular shielding. Combined photopeak ratio and Compton scatter residual plots for each measurement are shown in Fig. 6-Fig. 9 with shielding estimates tabulated in Table I. Combined bare with lead, tin and iron measurements were reasonably reconstructed, sufficiently informing users of rough shielding atomic number

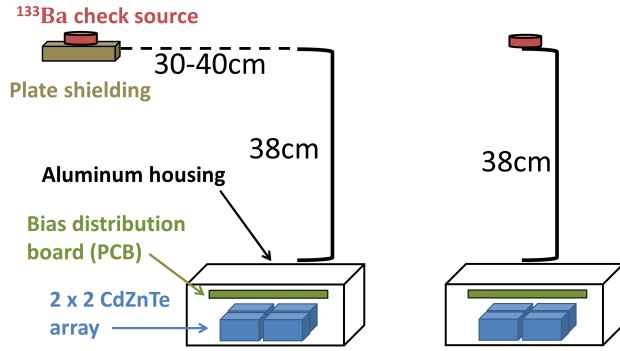


Fig. 4. (Left) Measurement schematic for shielded sources. Plate shielding was placed directly under the sources to insure the detector was fully shielded. Note the non-negligible amount of scattering material in the detector housing and bias distribution boards contributing to β . (Right) Measurement schematic for bare sources.

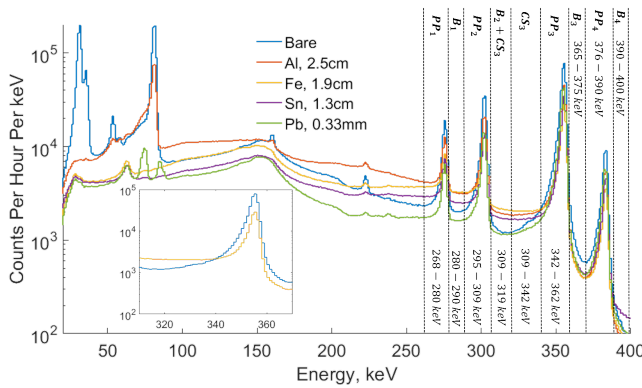


Fig. 5. Measured ^{133}Ba spectra for several shielding configurations. The boxed inset emphasizes the relative ratio between small-angle scatter and photopeak counts for the bare and iron measurements. Note the iron continuum is larger, from small-angle scatter within the shield, even though the bare photopeak has more counts. Photopeak, small-angle Compton scatter and background energy bins were labeled PP , CS and B respectively for each subscripted photopeak number.

and mass thickness in both the bare and shielded direction. Slight systematic bias was seen in the iron shielded case and may stem from naive background subtraction. Contrastingly, the reconstructed atomic number in the aluminum direction of the combined bare and aluminum measurement was drastically underestimated. However, the dotted bands of plausible residual fits contain many possible shielding combinations. This degenerate shielding behavior stems from gamma-ray attenuation changing slowly at high energies as a function of Z for low atomic number materials. Furthermore, naive background subtraction assuming a flat continuum degrades the small expected change in photopeak ratios shown in Fig. 10. Combined, this results in an ambiguously reconstructed Z as many element's expected photopeak ratios are plausible within measurement uncertainty. This illustrates that for technique to work the magnitude of the spectral modulation must be large compared to combined statistical and systematic errors in computing directional spectra. Limiting cases occur for low Z shields, where photopeak ratios are not heavily modulated, or for thick shields where few photons are recorded. Including

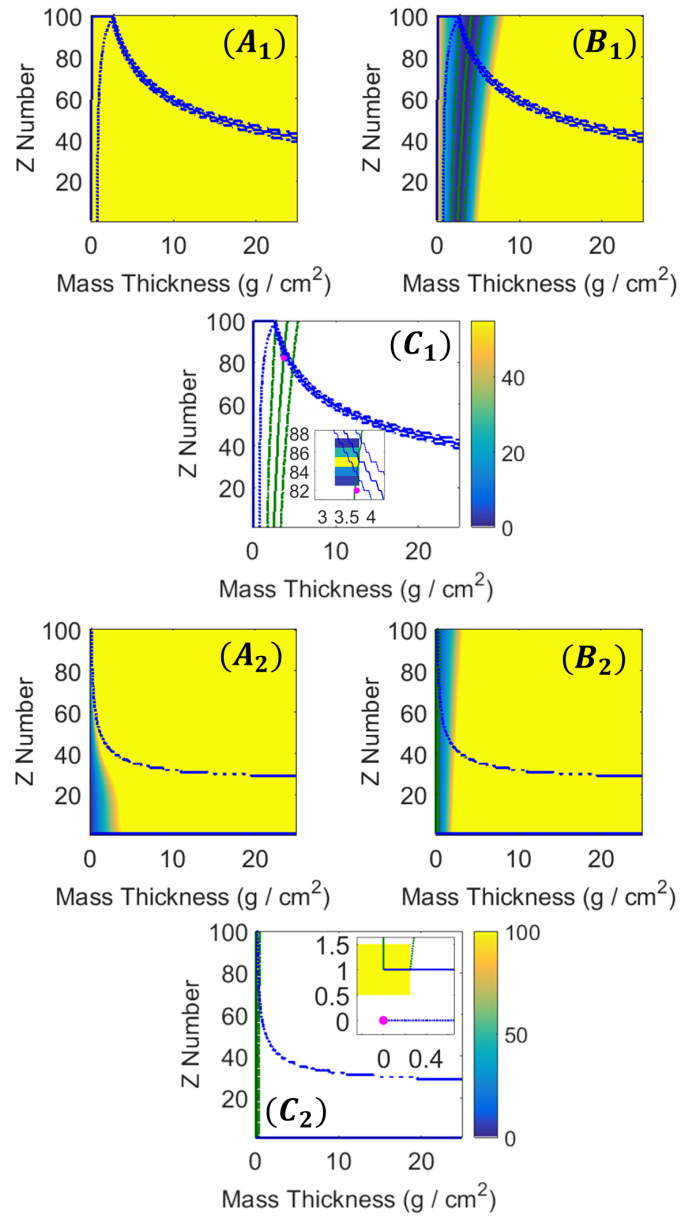


Fig. 6. Peak ratio residual (A), small-angle Compton scattering residual (B) and combined residuals (C) for counts reconstructed in lead shielded direction one (top) and bare direction two (bottom). Regions of good residual fit, corresponding to twice the minimum residual, are contained inside dashed lines. The inset figure shows uncertainties estimated via bootstrapping.

low energy peak ratios using the 81 keV ^{133}Ba emission would resolve this ambiguity as total attenuation changes more rapidly with atomic number at lower energies. This however requires combined Compton and coded aperture imaging as 81 keV gamma-rays do not produce many Compton imaged events in CdZnTe detectors. Despite this ambiguity the Compton scatter residual accurately predicts the aluminum shielding thickness while the bare source is accurately reconstructed.

Reconstructed uncertainties in shielding atomic number and mass thickness were quantified by processing many bootstrapped realizations of the initial measurements [19][20]. Bootstraps were taken with the same number of samples,

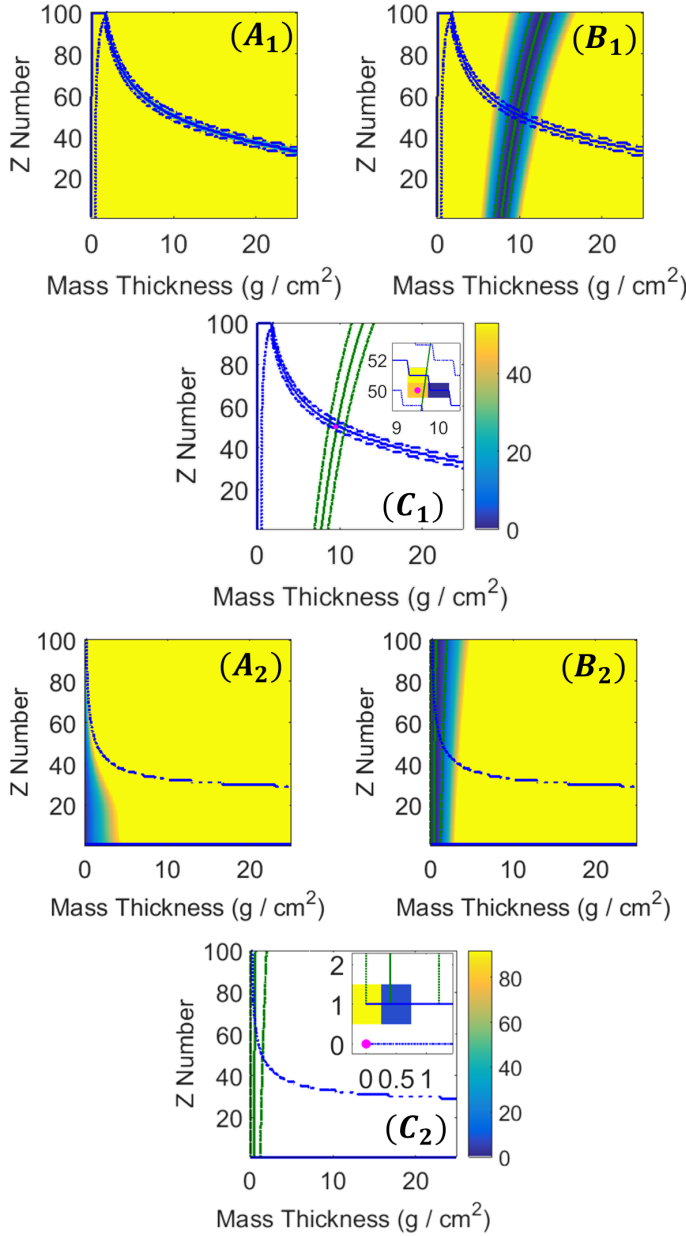


Fig. 7. Peak ratio residual (A), small-angle Compton scattering residual (B) and combined residuals (C) for counts reconstructed in tin shielded direction one (top) and bare direction two (bottom). Regions of good residual fit are contained inside dashed lines. The inset figure shows uncertainties estimated via bootstrapping.

taken with replacement, as events in the initial measurements. Bootstrapped results for the lead, tin, iron and aluminum shielded measurements are shown inset in Fig. 6-Fig. 9. Bootstrapped uncertainties fell within regions of plausible residual fit marked by dashed lines. This suggests that the plausible bounds, corresponding to twice the minimum residual fit, provided via the shielding reconstruction algorithm can be used to conservatively estimate uncertainty without the extreme computation expense of bootstrapping.

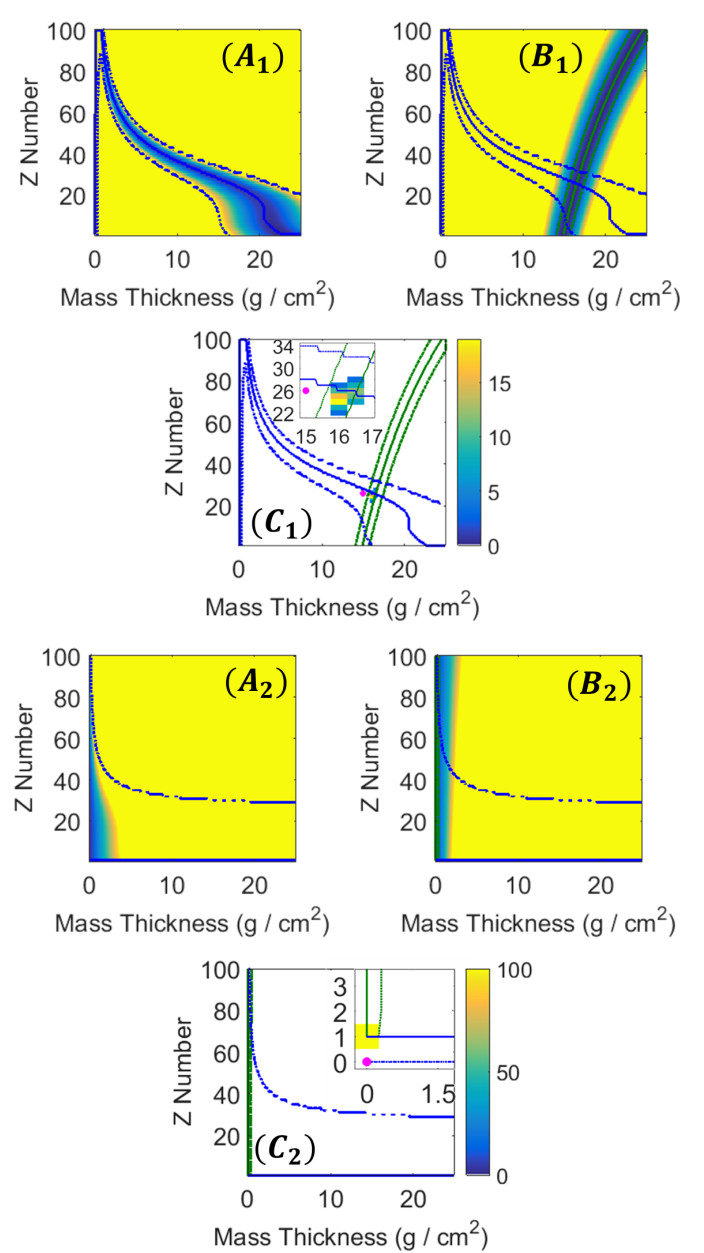


Fig. 8. Peak ratio residual (A), small-angle Compton scattering residual (B) and combined residuals (C) for counts reconstructed in iron shielded direction one (top) and bare direction two (bottom). Regions of good residual fit are contained inside dashed lines. The inset figure shows uncertainties estimated via bootstrapping.

TABLE I
TRUE AND ESTIMATED SHIELDING MASS THICKNESS AND ATOMIC NUMBER FOR EACH POSITION IN ALL MEASUREMENTS. ERROR BARS ARE STATISTICAL AND CALCULATED VIA BOOTSTRAPPING.

Shielding g/cm ² , Z	Pos. 1 True	Pos. 2 True	Pos. 1 Estimated	Pos. 2 Estimated
Al, Bare	6.9, 13	0.0, 0.0	6.9±0.1, 1.0±0.0	0.0±0.1, 1.0±0.0
Fe, Bare	15.0, 26	0.0, 0.0	16.5±0.1, 25.0±1.3	0.0±0.0, 1.0±0.0
Sn, Bare	9.5, 50	0.0, 0.0	9.7±0.1, 50.5±0.5	0.3±0.1, 1.0±0.0
Pb, Bare	3.7, 82	0.0, 0.0	3.7±0.1, 85±0.7	0.0±0.0, 1.0±0.0

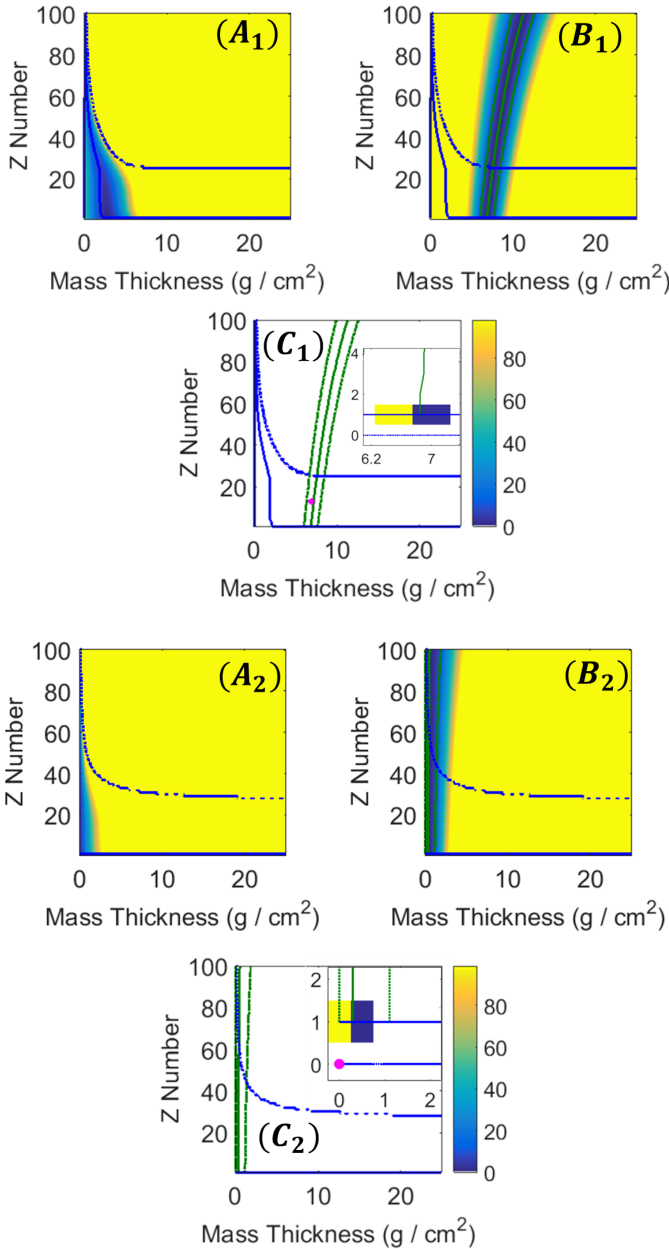


Fig. 9. Peak ratio residual (A), small-angle Compton scattering residual (B) and combined residuals (C) for counts reconstructed in aluminum shielded direction one (top) and bare direction two (bottom). Regions of good residual fit are contained inside dashed lines. The inset figure shows uncertainties estimated via bootstrapping. Note the general ambiguity is seen in aluminum Z number although Compton scattering correctly identifies shielding thickness.

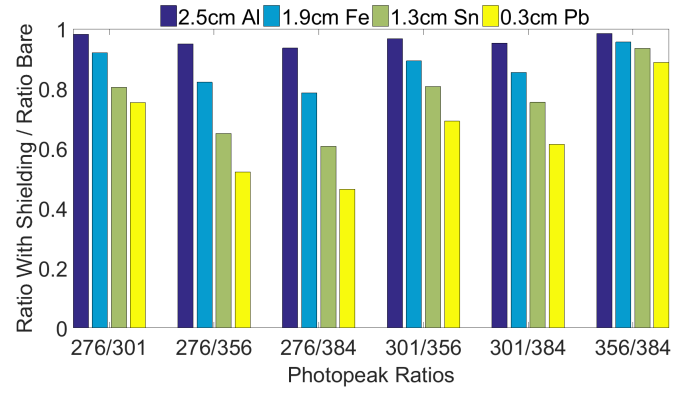


Fig. 10. Expected deviations from bare ^{133}Ba peak ratios for measured shielding configurations. Note that the aluminum shielded photopeak ratios do not greatly differ from the bare case. This complicates low Z measurements.

VII. DISCUSSION

The described directional shielding identification algorithm can be applied to spectrometers with any imaging modality that sufficiently detangles the spectral contribution of neighboring sources. Notably, the shielding identification algorithm will perform better with HPGc detectors due to the improved calculation of photopeak and small-angle scatter intensities from improved energy resolution and reduced low energy tailing. If multiple sources are separated by less than the system imaging resolution severe spectral contamination and therefore degraded shielding estimation is expected. The angular shielding identification algorithm can be readily extended to more than two point sources by simply selecting more regions of interest. Furthermore, spatially extended source shielding distributions can be characterized, given sufficient measurement statistics, if the shielding changes on spatial scales larger than imager resolution. Given long dwell times, reconstructions of complicated shielding distributions can be improved by tomographically combining multiple object views to ascertain 3D shielding distributions. Alternative imaging techniques, such as Stochastic Origin Ensembles (SOE) or Filtered Backprojection (FBP), may also be used to efficiently detangled directional spectra to estimate directional shielding [21][22].

VIII. CONCLUSION

Angular spectra returned by Compton imaging over specific energy windows with MLEM can be used in previously developed shielding detection algorithms to simultaneously estimate unknown shielding atomic numbers and mass thicknesses for multiple sources within a FOV. Iron, tin and lead shielded ^{133}Ba sources were accurately reconstructed with average standard error in relative atomic number and mass thickness of 1.5 and 0.6 g/cm^2 , respectively. Aluminum shielded sources were reconstructed with ambiguous atomic number but correct mass thickness due to the slowly changing total attenuation of low Z media and imperfect background subtraction. This ambiguity can be resolved by including low energy lines through coded aperture imaging.

ACKNOWLEDGMENT

The authors would like to thank their current colleagues in the Orion Radiation Measurement Group and past group members whose work they leverage. This material is based upon work supported by the National Science Foundation Graduate Research Fellowship under Grant No. DGE 1256260. The Orion Prototype has been developed under funding support from the US Department of Defense, Defense Threat Reduction Agency under award No. HDTRA1-12-C-0034. Any opinions, findings and conclusions or recommendations expressed in this material are those of the authors and do not necessarily reflect the views of the Defense Threat Reduction Agency.

REFERENCES

- [1] M. Streicher, S. Brown, Y. Zhu, D. Goodman, and Z. He, "A Method to Estimate the Atomic Number and Mass Thickness of Intervening Materials in Uranium and Plutonium Gamma-Ray Spectroscopy Measurements," *IEEE Transactions on Nuclear Science*, vol. 63, no. 5, pp. 2639–2648, 2016.
- [2] M. L. Galloway, "Characterization and Applications of a CdZnTe-Based Gamma-Ray Imager," Ph.D. dissertation, University of California, Berkley, 2014.
- [3] W. Wang, "Techniques and Applications of Compton Imaging for Position-Sensitive Gamma-Ray Detectors," Ph.D. dissertation, University of Michigan, 2011.
- [4] PHDS Co., "Germanium Gamma Ray Imaging Detectors," 2017. [Online]. Available: <http://phdsco.com>
- [5] C. G. Wahl, W. R. Kaye, W. Wang, F. Zhang, J. M. Jaworski, A. King, Y. A. Boucher, and Z. He, "The Polaris-H imaging spectrometer," *Nuclear Instruments and Methods A*, vol. 784, pp. 377–381, 2015.
- [6] S. M. Horne, G. G. Thoreson, L. A. Theisen, D. J. Mitchell, L. Harding, and A. Wendy, "GADRAS-DRF 18.5 User's Manual," Tech. Rep., 2014.
- [7] D. Xu and Z. He, "Gamma-ray energy-imaging integrated spectral deconvolution," *Nuclear Instruments and Methods A*, vol. 574, no. 1, pp. 98–109, 2007.
- [8] W. Wang, C. G. Wahl, J. M. Jaworski, and Z. He, "Maximum-likelihood deconvolution in the spatial and spatial-energy domain for events with any number of interactions," *IEEE Transactions on Nuclear Science*, vol. 59, no. 2, pp. 469–478, 2012.
- [9] W. Wang, S. Member, J. M. Jaworski, S. Member, W. R. Kaye, S. Member, and Z. He, "Applications of the Energy-Imaging Integrated Deconvolution Algorithm for Source Characterization," *IEEE Nuclear Science Symposium and Medical Imaging Conference, NSS/MIC*, pp. 1065–1068, 2009.
- [10] G. F. Knoll, *Radiation Detection and Measurement*. Hoboken:: Wiley, 2000.
- [11] O. Klein and Y. Nishina, "The scattering of light by free electrons according to Diracs new relativistic dynamics," *Nature*, vol. 122, p. 3072, 1928.
- [12] A. H. Compton, "A Quantum Theory of the Scattering of X-Rays By Light Elements," *Physical Review*, vol. 21, no. 5, pp. 483–502, 1923.
- [13] L. Sheep and Y. Vardi, "Maximum Likelihood Reconstruction for Emission Tomography," *IEEE Transactions on Medical Imaging*, vol. 1, no. 2, pp. 113–122, 1982.
- [14] C. E. Lehner, Z. He, and F. Zhang, " 4π Compton Imaging Using a 3-D Position-Sensitive CdZnTe Detector Via Weighted List-Mode Maximum Likelihood," *IEEE Transactions on Nuclear Science*, vol. 51, no. 4, pp. 1618–1624, 2004.
- [15] C. Wahl, "Imaging, Detection, and Identification Algorithms for Position Sensitive Gamma-Ray Detectors," Ph.D. dissertation, University of Michigan, 2011.
- [16] M. Streicher, Y. Zhu, F. Zhang, Y. A. Boucher, C. G. Wahl, H. Yang, and Z. He, "A Portable 2 x 2 Digital 3D CZT Imaging Spectrometer System," *IEEE Nuclear Science Symposium and Medical Imaging Conference*, pp. 2–4, 2014.
- [17] Y. Zhu and Z. He, "Performance of a 2-keV Digitizer ASIC for 3-D Position-Sensitive Pixelated Semiconductor Detectors," *IEEE Nuclear Science Symposium and Medical Imaging Conference*, pp. 4109–4112, 2012.
- [18] Y. Zhu, S. E. Anderson, and Z. He, "Sub-pixel position sensing for pixelated, 3-D position sensitive, wide band-gap, semiconductor, gamma-ray detectors," *IEEE Transactions on Nuclear Science*, vol. 58, no. 3, pp. 1400–1409, 2011.
- [19] B. Efron and R. Tibshirani, *An Introduction to the Bootstrap*. New York: CRC Press, 1998.
- [20] D. R. Haynor and S. D. Woods, "Resampling Estimates of Precision in Emission Tomography," *IEEE Transactions on Medical Imaging*, vol. 8, no. 4, pp. 337–343, 1989.
- [21] M. C. Hamel, J. K. Polack, A. Poitrasson-Rivière, M. Flaska, S. D. Clarke, S. A. Pozzi, A. Tomanin, and P. Peerani, "Stochastic image reconstruction for a dual-particle imaging system," *Nuclear Instruments and Methods A*, vol. 810, pp. 120–131, 2016.
- [22] J. Chu, M. Streicher, J. A. Fessler, and Z. He, "Unbiased Filtered Back-Projection in 4π Compton Imaging with 3D Position Sensitive Detectors," vol. 63, no. 6, pp. 2750–2756, 2016.